FULL RESEARCH ARTICLE

Thermal expansion behavior of Al–*x*Si alloys fabricated using selective laser melting

Y. D. Jia[1] · L. B. Zhang[1] · P. Ma[2] · S. Scudino[3] · G. Wang[1] · J. Yi[1] · J. Eckert[4,5] · K. G. Prashanth[4,6,7]

Abstract

Al–Si alloys are lightweight materials and show excellent mechanical and physical properties, making them appealing for automotive and aerospace industries applications. In this study, Al–(12–50 wt.%)Si alloys (nearly eutectic to hyper-eutectic compositions) were fabricated using a laser-based powder bed fusion process (LPBF) or selective laser melting technique (SLM). The microstructural evolution of the SLM Al–Si alloys as a function of increasing Si contents is investigated in detail. Refined Al and Si phases are observed and the mechanism of the refinement is discussed. In addition, the mechanical properties of the Al–Si alloy processed by casting and SLM were compared. Moreover, the influence of Si content and heating time on the coefficient of thermal expansion (CTE) of the alloys are investigated in detail, and their relationship between theoretical models and the experimental CTE values for the Al–Si alloys will be discussed and compared.

Keywords Selective laser melting · Al–si alloy · Microstructure · Thermal expansion

1 Introduction

Al–Si alloys are extensively used in automotive and aerospace industries due to their low weight combined with good mechanical and physical properties [1, 2]. The density

✉ P. Ma
    mapan@sues.edu.cn

✉ K. G. Prashanth
    kgprashanth@gmail.com

1   School of Materials Science and Engineering, Shanghai
    University, Shanghai 200444, China

2   School of Materials Engineering, Shanghai University
    of Engineering Science, Shanghai 201620, China

3   Solidification Processes and Complex Structures, Institute
    for Complex Materials, IFW Dresden, Helmholtzstraße 20,
    01069 Dresden, Germany

4   Erich Schmid Institute of Materials Science, Austrian
    Academy of Sciences, Jahnstraße 12, 8700 Leoben, Austria

5   Department Materials Physics, Montanuniversität Leoben,
    Jahnstraße 12, Jahnstraße 12, 8700 Leoben, Austria

6   Department of Mechanical and Industrial Engineering,
    Tallinn University of Technology, Ehitajate Tee 5,
    19086 Tallinn, Estonia

7   CBCMT, School of Mechanical Engineering, Vellore
    Institute of Technology, Vellore 632014, India

and coefficient of thermal expansion of the Al–Si alloys decrease with Si addition, affecting the thermal management and packaging applications [3]. The coefficient of thermal expansion of Al–Si alloys are influenced by the size and morphology of the eutectic or primary Si in the microstructure [4, 5]. It is known that the randomly distributed coarse Si phase acts as weak spots for crack initiation, which may lead to a pre-mature failure [6]. Acharya et al. [7] reported that the microstructure was refined and the mechanical property of the Al–20Si alloy was enhanced by addition γ-Al$_2$O$_3$ particles. Wang et al. [8] investigated the effect of Al–P–O master alloy on Si phase in hypereutectic Al–30Si alloy, and found that the primary Si was remarkably refined. As a consequence, the refinement of the Si phase in Al–Si alloys has been extensively investigated to improve their properties and to meet the ever-growing application demands in automotive, aerospace and electronic packaging industries [9, 10].

One of the most common methods for refining the Si phase in Al–Si alloys is the addition of secondary elements [11]. The addition and composition of such elements are easy to control and this technique has thus gained attention and wide application. However, the selection of the appropriate elements depends on the composition of the alloy. For example, in hypoeutectic Al–Si alloys, the most common refiners used are Na and Sr [11], which change the morphology of eutectic Si from a coarse plate-like to a

fine fibrous structure. Moreover, it has been reported that rare earth elements like Y [13], Yb [14], Eu [15] and Sc [16] can change the eutectic morphology from a coarse plate-like and acicular structure to fibrous or laminar. Increase of P from 0.0008 wt.% to 0.001 wt.% changes the appearance of primary Si from a large plate-like to a blocky morphology [17]. Moreover, it has been reported that the primary Si can be also refined through the inclusion of γ-Al_2O_3 [18], Ce [19] and Nb [20]. However, the elemental addition in the melt may oxidize both the melt and/or the elements at high temperature and the refinement effect may not be effectively controlled [4, 9]. Powder metallurgy and spray deposition processes have been developed as alternative routes for the manufacturing of Al–Si alloys in the past [21, 22]. Unfortunately, these processes have the following limitations: relatively high costs and complicated processing steps.

As an innovative rapid solidification technology, selective laser melting (SLM) fabricates components layer by layer through the selective melting of the powders as dictated by the CAD model [22–26]. A very small volume of melt pool combined with short laser interaction time offers a very high heating and cooling rates (10^4–10^8 K/s), resulting in a refined microstructure [27, 28]. Chien et al. [29] observed that coarse Si particles result in higher coefficient of thermal expansion (CTE), while finer Si particles may lower the CTE in Al–Si alloy. Hanemann et al. [30] investigated the CTE of AlSi10Mg alloy prepared by SLM technology, and found that the CTE is lower than the conventional cast sample, as a result of refinement microstructure. Additionally, SLM offers the production of objects with intricate shapes and complex geometries making SLM being widely used in both aeronautic and astronautic industries [28, 31].

Accordingly, in this work, the Al–Si alloys (12, 20, 35 and 50 wt.% Si) were fabricated by SLM of gas atomized Al–Si alloy powders. The microstructure evolution and the thermal expansion behavior were systematically investigated. The mechanism of the Si refinement and the influence of Si contents on the CTE of the alloys were studied.

2 Experimental

Al–Si alloy with four different Si compositions (from hypoeutectic to hypereutectic based on different application fields) were selected for investigation, as shown in Fig. 1. Gas atomized powders (~ 50 μm) with nominal compositions Al–12Si, Al–20Si, Al–35Si and Al–50Si (wt.%) were used in the SLM process. SLM 250HL from SLM Solutions Group AG, equipped with an Yb-fiber laser of maximum output 400 W was used for fabricating the Al–xSi samples. High-purity argon gas was used to ventilate the chamber before and during the building process to minimize oxygen contamination during processing. Cylinder samples (Φ 6 mm × 25 mm) were fabricated with stripe-type hatch and the laser beam followed bi-directional scanning. The SLM samples were processed using the following processing parameters: scanning speed 1455 mm/s, power 320 W for both volume and contour, layer thickness 50 μm, hatch spacing 110 μm and hatch style rotation of 73°.

The microstructures of the samples were characterized by optical microscopy (OM) using an Olympus optical

Fig. 1 Phase diagram of Al–Si binary alloy
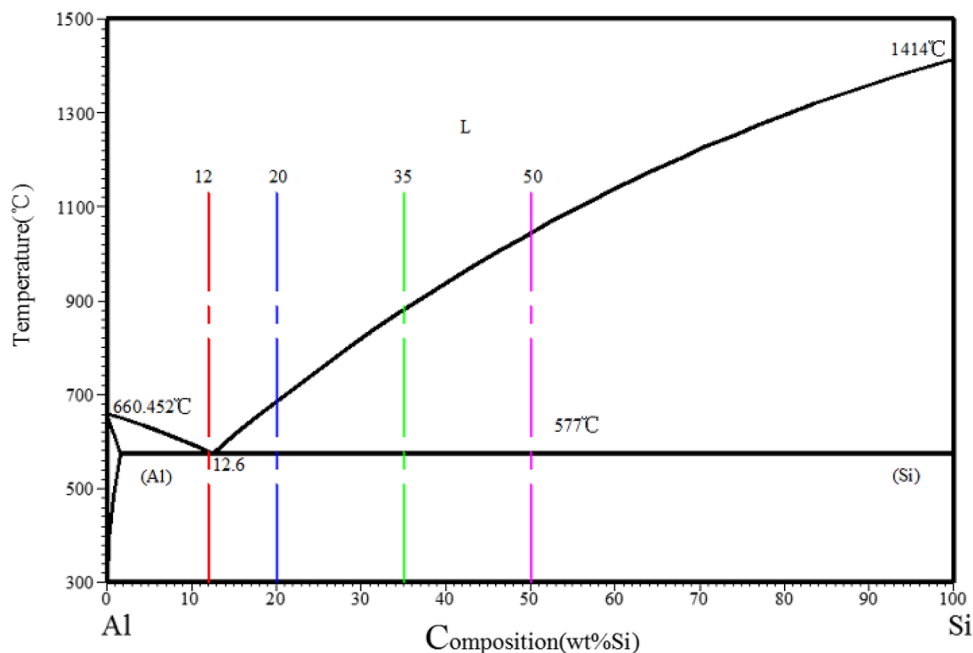
microscope (GX53F) and by scanning electron microscopy (SEM, Gemini 1530 microscope) after polishing and etching the samples in 0.5% HF solution. The phases present in the samples were analyzed by X-ray diffraction (XRD) using a D3290 PANalytical X'pert PRO diffractometer with Co-Kα radiation ($\lambda = 0.17889$ nm) in Bragg–Brentano configuration. The relative densities of the samples were determined using the Archimedes principle. The measurements for characterizing the thermal expansion behavior of the samples were carried out under argon atmosphere between room temperature and 773 K using a thermo-mechanical analysis equipment (NETZSCH DIL 402C) at heating and cooling rates of 5 K/min in two consecutive cycles. The size of the melt pool boundaries were measured from the microscopy images (OM/SEM). The distance between the centers of one melt pool to the other is measured as the effective melt pool size and the average values are given. A minimum of 20 melt pool sizes were measured randomly from at least 3–5 SEM/OM images and their average values are given in the manuscript. The dimensions of the Si particles are measured assuming the Si particles are spherical in nature. The size

of the particles are tabulated by measuring the approximate size of the Si particles from OM/SEM image using color contrast imaging (using Image J software) and a minimum of 75–100 Si particles were measured and their average is given in the manuscript.

3 Results and discussion

3.1 Microstructural investigation

Figure 2 shows the OM micrographs of the Al–12Si, Al–20Si, Al–35Si, and Al–50Si samples fabricated by SLM. Typical laser tracks with anisotropic microstructure were observed for the Al–12Si SLM samples (Fig. 2a). The microstructure of the sample can be divided into two parts, i.e., the melt pool borders with width $\sim 9 \pm 0.5$ μm (part I), and the track cores (part II) due to the differences in the thermal histories. The microstructure of the SLM alloy is normally affected by the heat generated by
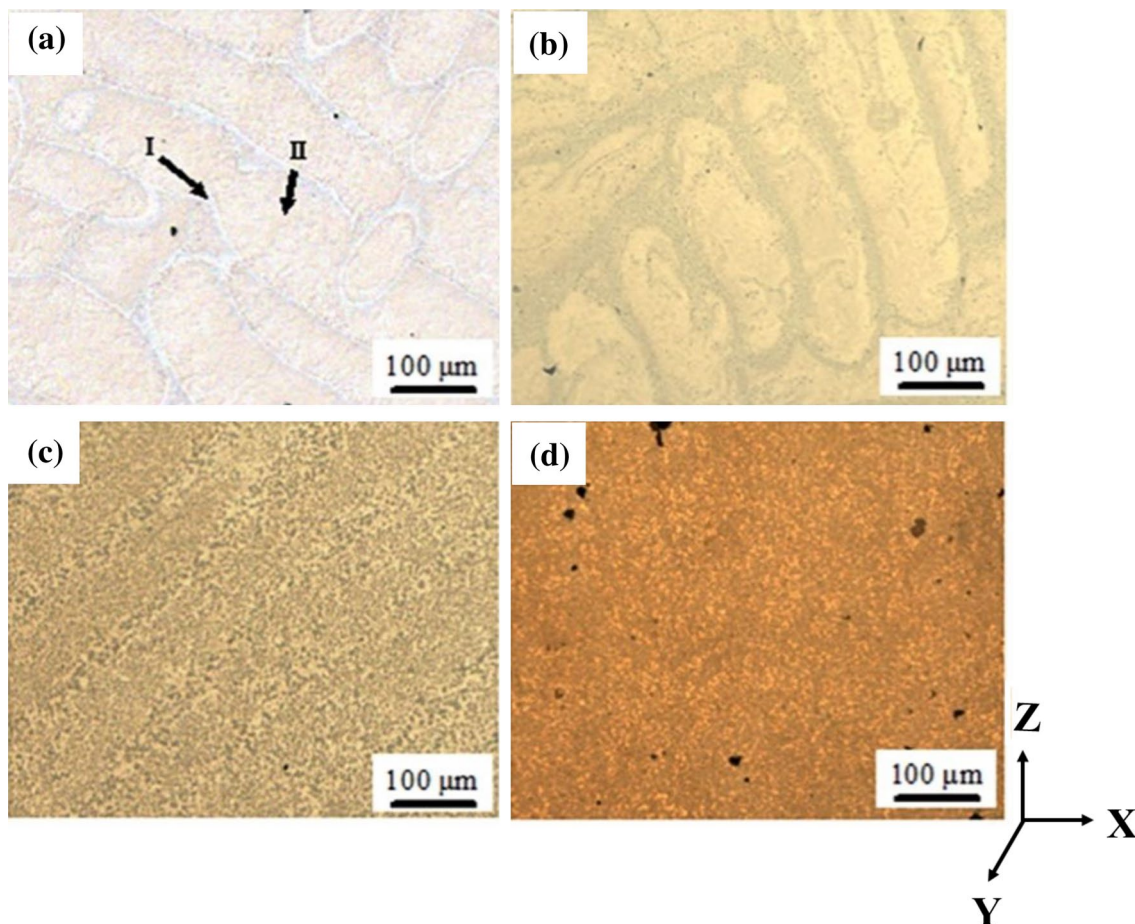

Fig. 2 Optical micrographs of the Al–Si alloys prepared by SLM. **a** Al–12Si, **b** Al–20Si, **c** Al–35Si and **d** Al–50Si

both the overlapping scan lines and the creation of the subsequent layers [28]. The melt pool borders (part I) are melted twice.

Figure 2b shows the microstructure of the SLM Al–20Si alloy, similar to the SLM-fabricated Al–12Si alloy, where typical laser tracks can be clearly seen. However, compared with the Al–12Si alloy, the amount of melt pool borders is larger and the size of the melt pool borders increases to 21 ± 1 μm. With increasing Si content, the size of the melt pool borders increases, and reaches 52 ± 3 μm, when the Si content is 35 wt.%. The track cores present a strip morphology, as shown in Fig. 2c. SLM Al–50Si microstructure becomes rather homogenous (Fig. 2d) where the melt pool borders and core cannot be distinguished. The melt pool borders become wider because of the existing primary Si phase, where primary Si is incompletely melted during the secondary melting, therefore, serving as nucleation sites for the secondary melting. The amount of primary Si increases with increasing Si content in the alloys, resulting in widened melt pool borders. When the content of Si reaches 50 wt.%, the microstructure is relatively homogenous due to the abundance of existing primary Si particles.

Figure 3 shows microstructures of the SLM fabricated Al–Si alloys, where refined Si phase is observed as a result of the high cooling rate. The diffusion of Si atoms is hindered and the growth of Si is limited. As observed in Fig. 3a–c, only eutectic Si with fibrous morphology can be found in the SLM Al–12Si alloy due to the low content of Si. The average thickness of the eutectic Si is 431 ± 10 nm in the melt pool borders and 130 ± 6 nm in the track cores. Figure 3d–f shows the microstructures of the SLM Al–20Si alloy, where larger polygonal Si particles are found in the melt pool borders (with size 1 ± 0.1 μm). The eutectic Si phase exhibits a fine fibrous morphology in the track cores. As the silicon content further increases to 35 wt.%, a large amount of primary Si phase appears in the solidified microstructure Fig. 3g–i. The eutectic silicon displays mainly a fine fibrous morphology, but part of the eutectic silicon transforms into a granular shape.

The average size of primary Si is 4.5 ± 0.4 μm and 2.4 ± 0.2 μm in the melt pool borders and track cores, respectively. With increasing Si content to 50 wt.%, polygonal-shaped primary Si is observed predominantly in the microstructure (Fig. 3j–l). The mean particle size of the primary Si phase is 5.8 ± 0.4 μm and 3.7 ± 0.3 μm in the melt pool borders and track cores, respectively. The fibrous eutectic silicon completely transforms into particles, which can be ascribed to the presence of enough primary Si particles in the Al–50Si alloy. The diffusion of residual Si atoms in the melt will be difficult due to the presence of the surrounding primary Si particles. Moreover, the primary silicon phase can serve as nucleation sites for Si atoms and it also helps in the modification of eutectic Si phase.

For comparison purposes, the typical microstructure of cast Al–xSi alloy are shown in Fig. 4. Here, we display the microstructures of the alloys with the lowest and the highest Si contents. As shown in Fig. 4a, the cast sample displays a continuous eutectic structure of Al and Si along with dispersed primary α-Al (bright dendrites) characteristic for the hypoeutectic compositions. The microstructure of cast Al–50Si alloy is composed of primary Si phase and of eutectic Al–Si. The primary Si particles, with polygonal and plate-like morphologies with size larger than 100 μm. The microstructures of the cast samples are completely different from the selective laser-melted counterparts.

The XRD patterns of the SLM Al–Si as a function of Si content show the typical diffraction peaks of α-Al and β-Si phases. It is reported that an Al(Si) super-saturated solid solution (SSSS) in Al–12Si alloy is formed due to the high cooling rates [28]. However, the diffraction peaks of the Al phase are shifted to higher angles with increasing Si content (Fig. 5) indicating the formation of a SSSS. Furthermore, the intensities of the Si (111) and (220) peaks increase with increasing Si content, which can be attributed to the increased volume fraction of free residual Si particles.

3.2 Mechanical property and CTE of the SLM Al–Si alloys

Figure 6 shows the room-temperature compression stress–strain curves of the Al–12Si and Al–50Si specimens prepared by SLM and by casting here. The SLM samples display compression and yield strength of about 726.7 and 506.8 MPa for Al–12Si alloy. The compression and yield strength of as cast Al–12Si alloy is 488.0 and 331.1 MPa. The SLM samples present yield and compression strength of about 731.64 and 666.74 MPa for Al–50Si alloy, respectively, which are much higher than the corresponding values of the cast material. The increased compression strength of the SLM samples may be attributed to the refined microstructural effects, such as the morphology, size and distribution of the Al and Si phases, as analyzed by Prashanth et al. [32–35] and Ma et al. [36].

The CTE can be expressed as the change in the dimensions of a material as a function of temperature [37]. The variation of the CTEs for the SLM Al–xSi alloys as a function of Si content show similar trend with increasing temperature (Fig. 7). The CTE of the material is related to the bonding force between the atoms and the CTE increases with decreasing bonding force [38]. With increasing temperature, the thermal motion of the Al atoms increases, and the Al–Si interfacial bonding force decreases, which results in an increase of CTE. Moreover, it is found that the CTE decreases with increasing amount of Si in the alloy, which is mainly because the CTE of Si is much lower than that of Al (Table 1). However, a distinct peak is observed for
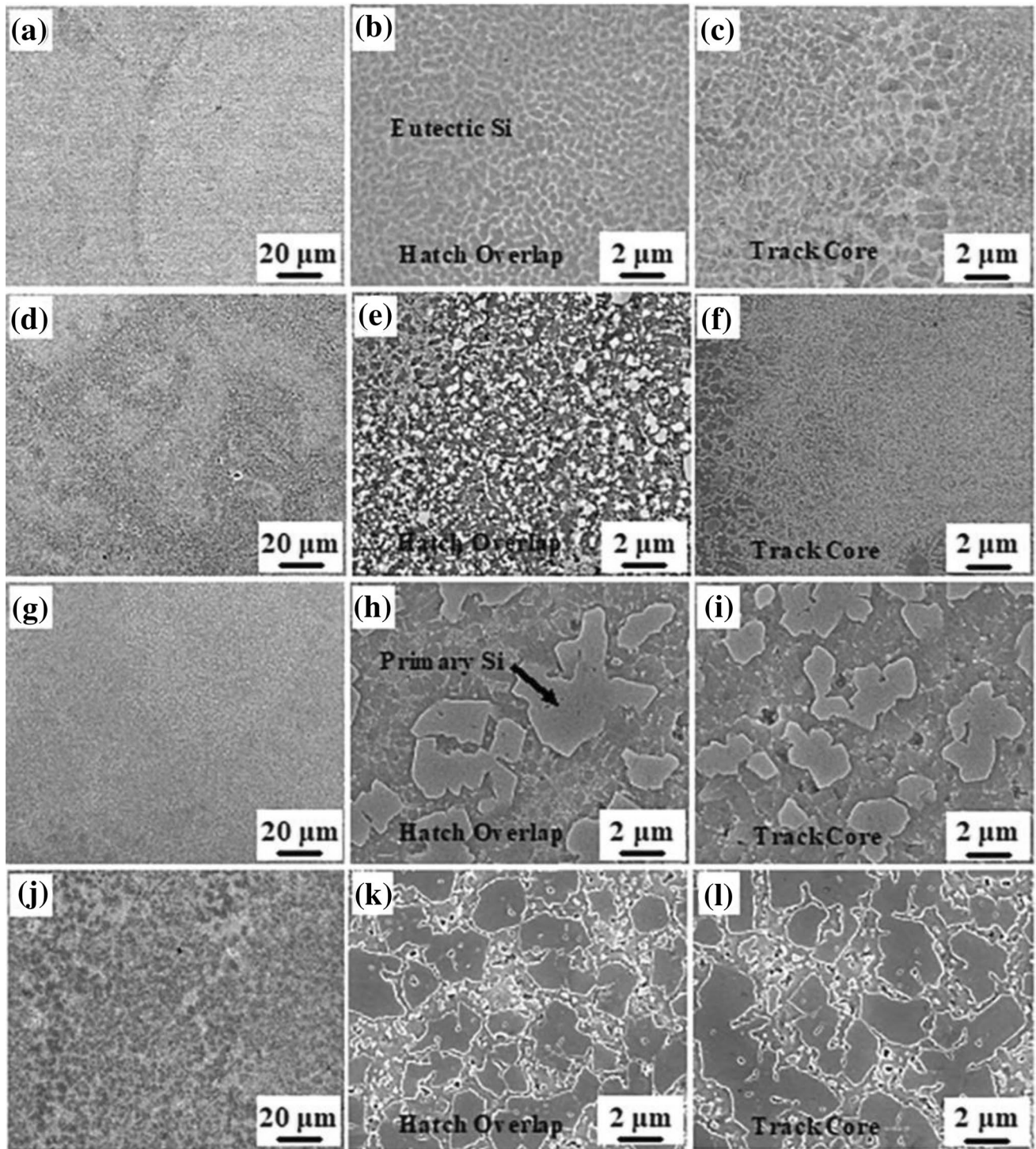
Fig. 3 Scanning electron microscopy images of the SLM fabricated Al–Si alloys. **a–c** Al–12Si, **d–f** Al–20Si, **g–i** Al–35Si and **j–l** Al–50Si

the Al–12Si alloy, which may be due to the formation of a SSSS. During the heating step, Si atoms precipitate from the Al matrix and lead to a rapid expansion of the lattice, which corresponds to the CTE peak [9, 39]. With further increasing temperature, the CTE curve becomes rather flat, which is caused by re-dissolution of a certain amount of Si in the Al matrix. The increased solid solubility of Si in Al at higher temperatures leads to a decrease CTE's of the gradient as a result of the smaller atomic radius of Si than Al [9]. The temperature range of the CTE peak increases and the

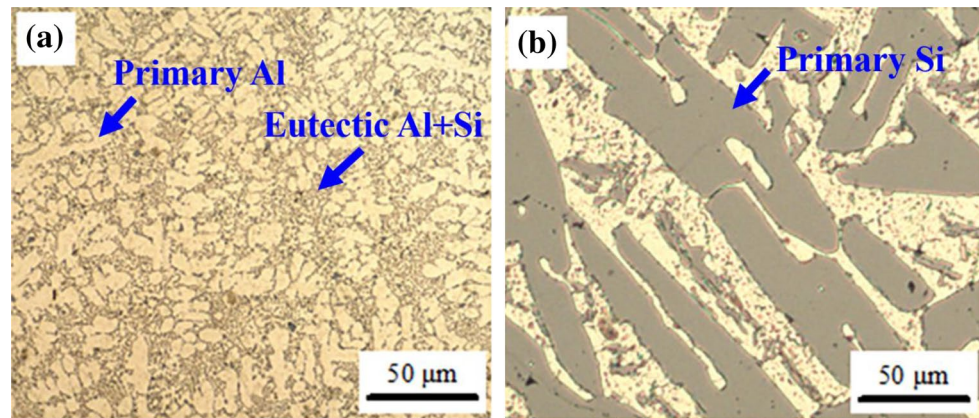**Fig. 4** Microstructures of as cast **a** Al–12Si alloy, **b** Al–50Si alloy

Fig. 5 XRD patterns of the SLM Al–Si alloys. **a** Al–12Si, **b** Al–20Si, **c** Al–35Si, **d** Al–50Si
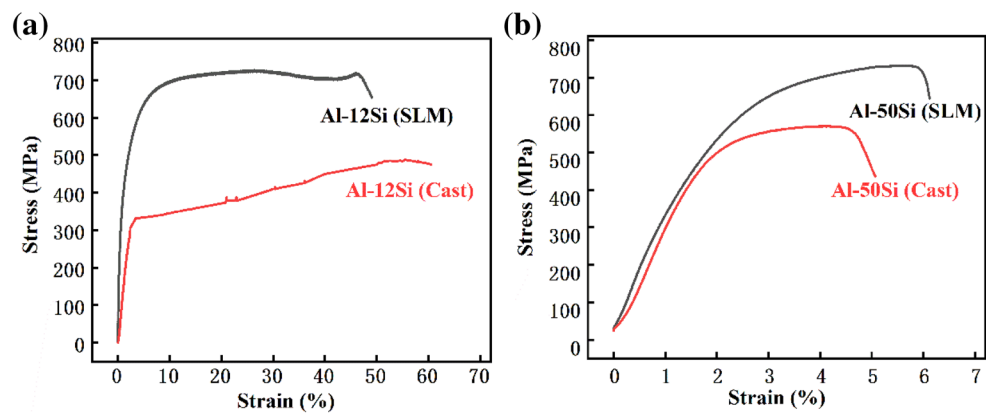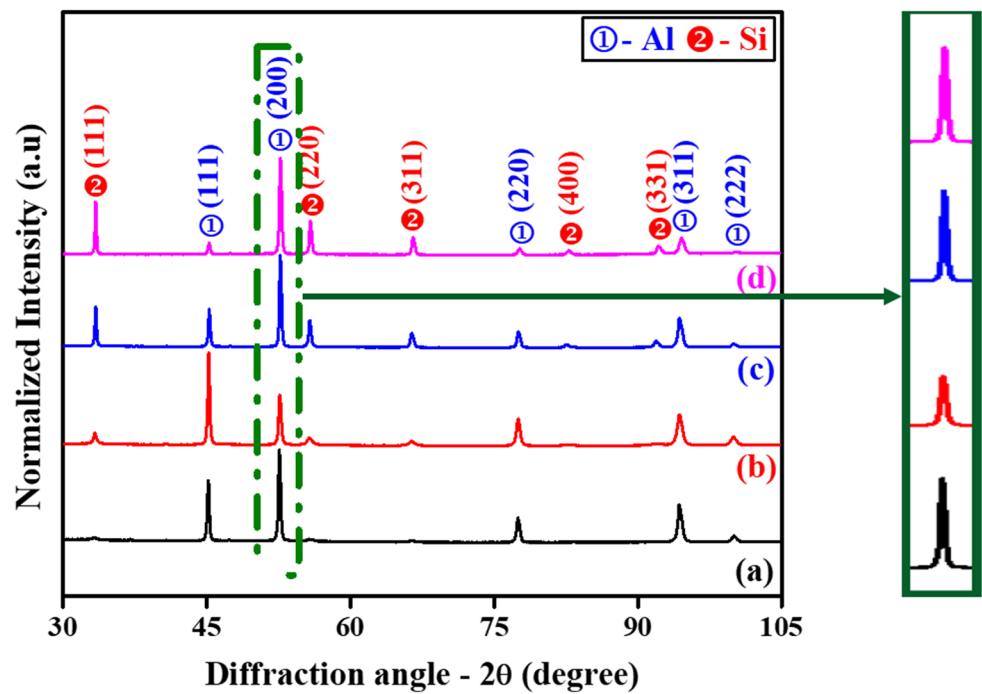

Fig. 6 Room-temperature compression tests of the cast and as-prepared SLM Al–Si samples. **a** Al–12Si alloy, **b** Al–50Si alloy
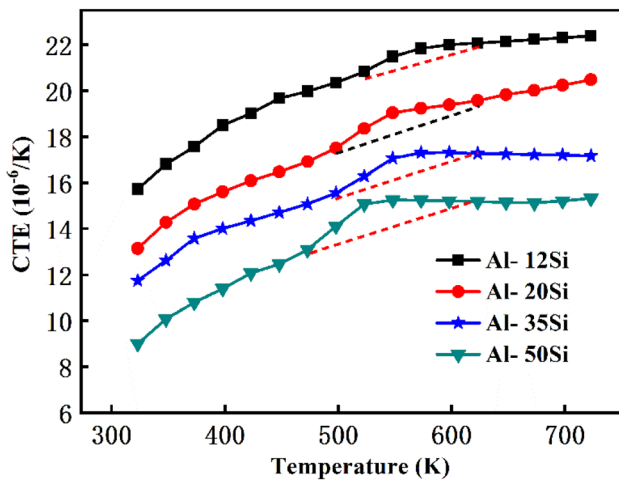
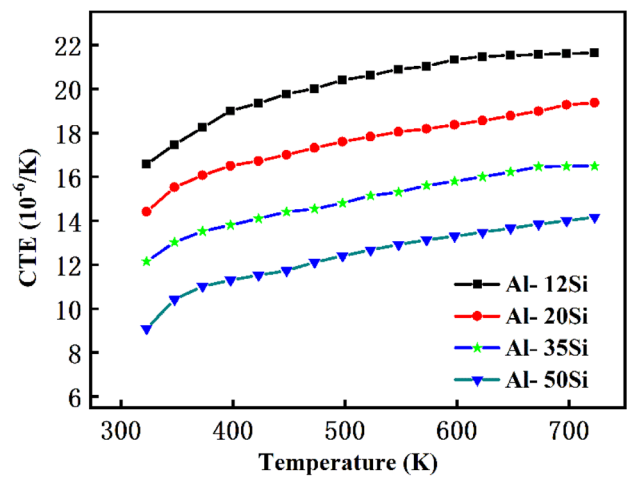**Fig. 7** CTE curves of the SLM-fabricated Al–Si alloys

Fig. 8 Effect of re-heating on the CTE curves of the SLM Al–Si alloys

peak temperature decreases with increasing Si content, due to precipitation of Si from SSSS [40]. With increasing Si content, more nucleation sites are provided, resulting in a rapid precipitation of Si atoms and an accelerated expansion of the Al matrix.

The CTE of all the alloys increase linearly at low temperatures and show a relatively sluggish increase at high temperatures during the secondary heating process (Fig. 8). This phenomenon can be ascribed to the combined effects of solubility of Si in Al and the change of internal stresses on the matrix with increasing temperature. The solid solubility of Si in Al increases with increasing temperature (above 523 K), which causes a negative effect on the CTE, because the lattice parameter of Al decreases with the increment of Si solubility [41–43]. In addition, large residual thermal stresses will be generated in the material during cooling due to the CTE mismatch between the Al and Si [44, 45]. Compressive residual stresses are observed on the Si particles and as tensile stress on the Al matrix. With increasing temperature, the matrix expands and the tensile stress decreases and when the tensile stress drops to zero, a new compressive stress on the matrix is induced resulting in a

decrease of the CTE of the matrix. The influence of the Si particles on the CTE of the alloy can be ignored because of the large modulus and strength of Si. It is worth noting that no CTE peaks are visible for the second heating process, corroborating that the peak corresponds to the precipitation of Si from SSSS (Fig. 9).

3.3 Theoretical models of the CTE

For simplicity, SLM Al–Si alloys can be treated as Al-matrix composites reinforced with Si particles [9]. Based on assumptions, several theoretical and numerical studies have provided expressions for the estimation of the CTE in particle-reinforced composites. In this work, the Turner and Schapery' models are used to investigate the temperature-dependent CTE behavior of SLM Al–Si alloys. The Turner model [46] considers uniform hydrostatic stresses that are assumed insufficient to disrupt the composite. The reinforcement and the matrix in the composite change at the same rate with temperature as the whole composite with negligible shear deformation. Moreover, the Turner

Table 1 Temperature dependence of the physical properties of Al and Si [8]

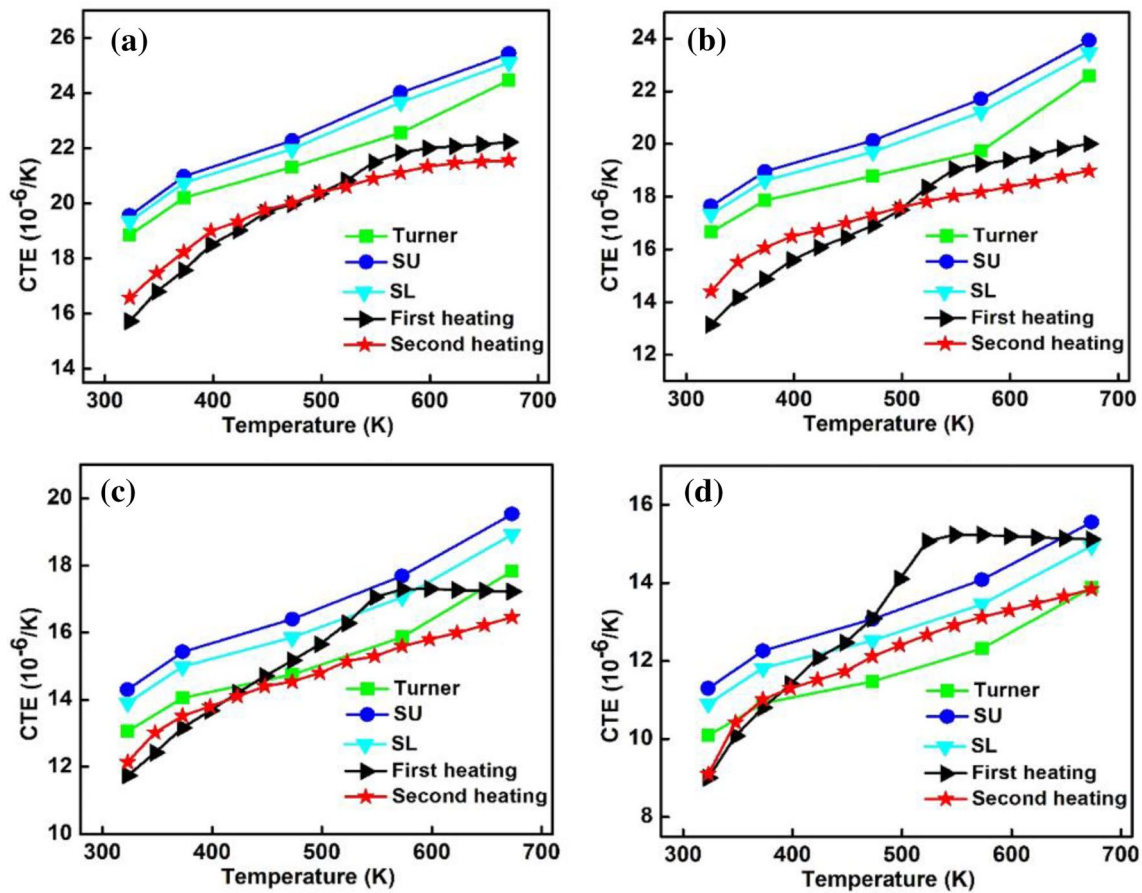| Temperature (K)	Al			Si		
	Elastic modulus (E/GPa)	Possion's ratio (ν)	CTE (α/$\times 10^{-6}$/K)	Elastic modulus (E/GPa)	Possion's ratio (ν)	CTE (α/$\times 10^{-6}$/K)
323	69.2	0.33	22.6	163	0.22	2.5
373	67.6	0.33	24.2	162		3.0
473	64.0	0.33	25.7	161		3.4
573	59.8	0.34	27.7	160		3.6
673	54.9	0.36	30.4	156		3.8
773	49.9	0.38	31.7	157		4.0

Fig. 9 Comparisons of theoretical and experimental CTE of the Al–Si alloys as-prepared (first heating) and re-heating (second heating) SLM samples: **a** Al–12Si, **b** Al–20Si, **c** Al–35Si and **d** Al–50Si. SU and SL are the upper and lower bounds from the Schapery model

model does not account for the angularity and the distribution of the reinforcement and gives the CTE of a composite as

$$\alpha = \frac{\alpha_p V_p K_p + \alpha_m V_m K_m}{V_p K_p + V_m K_m}, \tag{1}$$

where α is the CTE (10^{-6}/K), V is the volume fraction (vol.%), and the subscripts m and p refer to matrix and reinforcement, respectively. K is the bulk modulus, which can be expressed as:

$$K = \frac{E}{3(1-2\upsilon)} \quad \text{shear.} \tag{2}$$

E and ν denote Young's modulus and Poisson's ratio, respectively, which are provided in Table 1.

The Schapery' model takes the stress interaction between the components into account, assume particles are spherical in shape and wetted by a uniform, isotropic, homogenous matrix layer; the CTE can be expressed as [47]

$$\alpha_c = \alpha_p + (\alpha_m - \alpha_p) \times \frac{K_m(K_p - K_c)}{K_c(K_p - K_m)}. \tag{3}$$

The K_c value is obtained from the Hashin's bounds. Therefore, only the upper and lower bounds of K_c are known in a given case.

$$K_c^{lower} = K_m + \frac{V_p}{\frac{1}{K_p - K_m} + \frac{V_m}{K_m + \frac{4G_m}{3}}}, \tag{4}$$

$$K_c^{upper} = K_p + \frac{V_m}{\frac{1}{K_m - K_p} + \frac{V_p}{K_p + \frac{4G_p}{3}}}, \tag{5}$$

where G is the shear modulus (GPa), which can be calculated by:

$$G = \frac{E}{2(1+\nu)}. \tag{6}$$

For the first heating, the CTE values of the SLM Al–Si alloys are significantly different from the predictions of the theoretical models. This phenomenon is mainly attributed to the fact that the theoretical models neglect the formation of SSSS and precipitation behavior and all the hypotheses are based on a composite just modified by the presence of particles. Moreover, the CTE values of the Al–12Si and Al–20Si alloys during the second heating are lower than the ones predicted by the Turner and Schapery models, which can be ascribed to SLM-specific microstructures, where a large amount of fibrous eutectic silicon exists in these alloys, which is in contradiction with the theoretical models. With increasing amount of Si, the CTE values of the Al–35Si alloy during the second heating are in good agreement with the Turner model in the temperature range between 373 and 573 K. With further increasing Si content, the amount of fibrous eutectic silicon phase decreases and the amount of granular primary silicon increases, in accordance with the theoretical models. The CTE values for the SLM alloy during the second heating lie between the Schapery model and the Turner model. When the Si content reaches 50 wt.%, uniformly distributed granular primary silicon is formed, where this microstructure is closer to the assumptions made in the Schapery model and the CTE coincides better with the model predictions.

4 Conclusions

A series of Al–(12–50 wt.%)Si alloys were fabricated by SLM. The Si phases are refined in size due to the very high cooling rates. With increasing Si content, the size of the melt pool borders becomes wider, and the morphology of the eutectic Si changes from a fibrous to a particle morphology due to increased nucleation sites during the solidification. Peaks in the CTE curves are observed for the SLM alloys as a result of the formation of a SSSS of Al(Si), and the area of the CTE peaks increases with increasing amount of Si as a result of the accelerated precipitation of Si from the Al matrix. The consistence between the experimentally measured CTE and theoretical models is mainly determined by the morphology of the Si phase.

Compliance with ethical standards

References

1. Jung JG, Ahn TY, Cho YH, Kim SH, Lee JM (2018) Synergistic effect of ultrasonic melt treatment and fast cooling on the refinement of primary Si in a hypereutectic Al–Si alloy. Acta Mater 144:31–40. https://doi.org/10.1016/j.actamat.2017.10.039
2. Zhang SK, Ma P, Jia YD, Yu ZS, Sokkalingam R, Shi XR, Ji PC, Eckert J, Prashanth KG (2019) Microstructure and mechanical properties of Al-(12–20)Si Bi-material fabricated by selective laser melting. Mater 12:2126. https://doi.org/10.3390/ma12132126
3. Hanemann T, Carter LN, Habschied M, Adkins NJE, Attallah MM, Heilmaier M (2019) In-situ alloying of AlSi10Mg + Si using selective laser melting to control the coefficient of thermal expansion. J Alloys Compd 795:8–18. https://doi.org/10.1016/j.jallcom.2019.04.260
4. Li XP, Wang XJ, Saunders M, Suvorova A, Zhang LC, Liu YJ, Fang MH, Huang ZH, Sercombe TB (2015) A selective laser melting and solution heat treatment refined Al–12Si alloy with a controllable ultrafine eutectic microstructure and 25% tensile ductility. Acta Mater 95:74–82. https://doi.org/10.1016/j.actamat.2015.05.017
5. Kang N, Coddet P, Chen CY, Wang Y, Liao HL, Coddet C (2016) Microstructure and wear behavior of in-situ hypereutectic Al-high Si alloys produced by selective laser melting. Mater Des 99:120–126. https://doi.org/10.1016/j.matdes.2016.03.053
6. Prashanth KG (2019) Work hardening in selective laser melted Al-12Si alloy. Mater Des Process Commun 1:e46. https://doi.org/10.1002/mdp2.46
7. Acharya M, Mandal A (2019) Individual and synergistic effect of gamma alumina (γ-Al$_2$O$_3$) and strontium on microstructure and mechanical properties of Al−20Si alloy. Trans Nonferr Metal Soc 29:1353–1364. https://doi.org/10.1016/S1003-6326(19)65042-9
8. Wang K, Lu X, Zhu YM, Jiang HY, Wang QD, Ye B, Ding WJ (2019) In-situ synthesis of novel Al–P–O master alloy and its refinement and modification effects on Si phases in hypereutectic Al–30Si alloys. Mater Character 157:109900. https://doi.org/10.1016/j.matchar.2019.109900
9. Jia YD, Ma P, Prashanth KG, Wang G, Yi J, Scudino S, Cao FY, Sun JF, Eckert J (2017) Microstructure and thermal expansion behavior of Al-50Si synthesized by selective laser melting. J Alloys Compd 699:548–553. https://doi.org/10.1016/j.jallcom.2016.12.429
10. Choi HS, Konishi H, Li XC (2012) Al$_2$O$_3$ nanoparticles induced simultaneous refinement and modification of primary and eutectic Si particles in hypereutectic Al–20Si alloy. Mater Sci Eng A 541:159–165. https://doi.org/10.1016/j.msea.2012.01.131
11. Chen ZN, Kang HJ, Fan GH, Li JH, Lu YP, Jie JC, Zhang YB, Li TJ, Jian XG, Wang TM (2016) Grain refinement of hypoeutectic Al–Si alloys with B. Acta Mater 120:168–178. https://doi.org/10.1016/j.actamat.2016.08.045
12. McDonald SD, Kazuhiro N, Dahle AK (2004) Eutectic nucleation in Al–Si alloys. Acta Mater 52:4273–4280. https://doi.org/10.1016/j.actamat.2004.05.043
13. Li B, Wang HW, Jie JC, Wei ZJ (2011) Effects of yttrium and heat treatment on the microstructure and tensile properties of Al–7.5Si–0.5Mg alloy. Mater Des 32:1617–1622. https://doi.org/10.1016/j.matdes.2010.08.040
14. Li B, Wang HW, Jie JC, Wei ZJ (2011) Microstructure evolution and modification mechanism of the ytterbium modified Al–7.5%Si–0.45%Mg alloys. J Alloys Compd 509:3387–3392. https://doi.org/10.1016/j.jallcom.2010.12.081
15. Li JH, Wang XD, Ludwig TH, Tsunekawa Y, Arnberg L, Jiang JZ, Schumacher P (2015) Modification of eutectic Si in Al–Si

alloys with Eu addition. Acta Mater 84:153–163. https://doi.org/10.1016/j.actamat.2014.10.064

16. Prukkanon W, Srisukhumbowornchai N, Limmaneevichitr CW (2009) Modification of hypoeutectic Al–Si alloys with scandium. J Alloys Compd 477:454–460. https://doi.org/10.1016/j.jallcom.2008.10.016

17. Cao FY, Jia YD, Prashanth KG, Ma P, Liu JS, Scudino S, Huang F, Eckert J, Sun JF (2015) Evolution of microstructure and mechanical properties of as-cast Al–50Si alloy due to heat treatment and P modifier content. Mater Des 74:150–156. https://doi.org/10.1016/j.matdes.2015.03.008

18. Li QL, Xia TD, Lan YF, Zhao WJ, Fan L, Li PF (2013) Effect of in situ γ-Al2O3 particles on the microstructure of hypereutectic Al–20%Si alloy. J Alloys Compd 577:232–236. https://doi.org/10.1016/j.jallcom.2013.04.043

19. Li QL, Xia TD, Lan YF, Zhao WJ, Fan L, Li PF (2013) Effect of rare earth cerium addition on the microstructure and tensile properties of hypereutectic Al–20%Si alloy. J Alloys Compd 562:25–32. https://doi.org/10.1016/j.jallcom.2013.02.016

20. Xu CL, Jiang QC, Yang YF, Wang HY, Wang JG (2006) Effect of Nd on primary silicon and eutectic silicon in hypereutectic Al–Si alloy. J Alloys Compd 422:L1–L4. https://doi.org/10.1016/j.jallcom.2005.03.128

21. Cui C, Schulz A, Schimanski K, Zoch HW (2009) Spray forming of hypereutectic Al–Si alloys. J Mater Process Technol 209:5220–5228. https://doi.org/10.1016/j.jmatprotec.2009.03.009

22. Ma P, Zou CM, Wang HW, Scudino S, Song KK, Khoshkhoo MS, Wei ZJ, Eckert KU (2013) Structure of GP zones in Al–Si matrix composites solidified under high pressure. Mater Lett 109:1–4. https://doi.org/10.1016/j.matlet.2013.06.075

23. Prashanth KG, Damodaram R, Scudino S, Wang Z, Rao KP, Eckert J (2014) Friction welding of Al–12Si parts produced by selective laser melting. Mater Des 57:632–637. https://doi.org/10.1016/j.matdes.2014.01.026

24. Prashanth KG, Scudino S, Eckert J (2017) Defining the tensile properties of Al–12Si parts produced by selective laser melting. Acta Mater 126:25–35. https://doi.org/10.1016/j.actamat.2016.12.044

25. Olakanmi EO, Cochrane RF, Dalgarno KW (2015) A review on selective laser sintering/melting (SLS/SLM) of aluminium alloy powders: processing, microstructure, and properties. Prog Mater Sci 74:401–477. https://doi.org/10.1016/j.pmatsci.2015.03.002

26. Martin JH, Yahata BD, Hundley JM, Mayer JA, Schaedler TA, Pollock TM (2017) 3D printing of high-strength aluminium alloys. Nature 549:365–369. https://doi.org/10.1016/j.jallcom.2018.02.272

27. Ma P, Jia YD, Prashanth KG, Scudino S, Yu ZS, Eckert J (2016) Microstructure and phase formation in Al–20Si–5Fe–3Cu–1Mg synthesized by selective laser melting. J Alloys Compd 657:430–435. https://doi.org/10.1016/j.jallcom.2015.10.119

28. Olakanmi EO (2013) Selective laser sintering/melting (SLS/SLM) of pure Al, Al–Mg, and Al–Si powders: effect of processing conditions and powder properties. J Mater Process Technol 213:1387–1405. https://doi.org/10.1016/j.jmatprotec.2013.03.009

29. Chien CW, Lee SL, Lin JC, Jahn MT (2002) Effects of Si_p size and volume fraction on properties of Al/Si_p composites. Mater Lett 52:334–341. https://doi.org/10.1016/S0167-577X(01)00418-9

30. Hanemann T, Habschied CLN, Adkins NJE, Attallah MM, Heilmaier M (2019) In-situ alloying of AlSi10Mg + Si using selective laser melting to control the coefficient of thermal expansion. J Alloys Compd 795:8–18. https://doi.org/10.1016/j.jallcom.2019.04.260

31. Aboulkhair NT, Simonelli M, Parry L, Ashcroft I, Tuck C, Hague R (2019) 3D printing of aluminium alloys: additive manufacturing of aluminium alloys using selective laser melting. Prog Mater Sci 106:100578. https://doi.org/10.1016/j.pmatsci.2019.100578

32. Prashanth KG, Scudino S, Klauss H, Surreddi KB, Löber L, Wang Z, Chaubey AK, Kühn U, Eckert J (2014) Microstructure and mechanical properties of Al-12Si produced by selective laser melting: effect of heat treatment. Mater Sci Eng A 590:153–160. https://doi.org/10.1016/j.msea.2013.10.023

33. Prashanth KG, Scudino S, Chaubey AK, Loeber L, Wang P, Attar H, Schimansky FP, Pyczak F, Eckert J (2016) Processing of Al-12Si-TNM composites by selective laser melting and evaluation of compressive and wear properties. J Mater Res 31:55–65. https://doi.org/10.1557/jmr.2015.326

34. Suryawanshi J, Prashanth KG, Scudino S, Eckert J, Prakash O, Ramamurty R (2016) Simultaneous enhancements of strength and toughness in an Al-12Si alloy synthesized using selective laser melting. Acta Mater 115:285–294. https://doi.org/10.1016/j.actamat.2016.06.009

35. Rathod HJ, Nagaraju T, Prashanth KG, Ramamurty U (2019) Tribological properties of selective laser melted Al-12Si alloy. Tribo Int 137:94–101. https://doi.org/10.1016/j.triboint.2019.04.038

36. Ma P, Prashanth KG, Scudino S, Jia YD, Wang HW, Zou CM, Wei ZJ, Eckert J (2014) Influence of annealing on mechanical properties of Al-20Si processed by selective laser melting. Metals 4:28–36. https://doi.org/10.3390/met4010028

37. Elomari S, Skibo MD, Sundarrajan A, Richards H (1998) Thermal expansion behavior of particulate metal-matrix composites. Compos Sci Technol 58:369–376. https://doi.org/10.1016/S0266-3538(97)00124-3

38. Arpón R, Molina JM, Saravanan RA, García-Cordovilla C, Louis E, Narciso J (2003) Thermal expansion behaviour of aluminium/SiC composites with bimodal particle distributions. Acta Mater 51:3145–3156. https://doi.org/10.1016/S1359-6454(03)00126-5

39. Wei ZJ, Ma P, Wang HW, Zou CM, Scudino S, Song KK, Prashanth KG, Jiang W, Eckert J (2015) The thermal expansion behaviour of SiCp/Al-20Si composites solidified under high pressures. Mater Des 65:387–394. https://doi.org/10.1016/j.matdes.2014.08.070

40. Ma P, Zou CM, Wang HW, Scudino S, Fu BG, Wei ZJ, Kühn U, Eckert J (2014) Effects of high pressure and SiC content on microstructure and precipitation kinetics of Al-20Si alloy. J Alloys Compd 586:639–644. https://doi.org/10.1016/j.jallcom.2013.10.128

41. Huber T, Degischer HP, Lefranc G, Schmitt T (2006) Thermal expansion studies on aluminium-matrix composites with different reinforcement architecture of SiC particles. Compos Sci Technol 66:2206–2217. https://doi.org/10.1016/j.compscitech.2005.12.012

42. Chang JY, Moon I, Choi CS (1998) Refinement of cast microstructure of hypereutectic Al-Si alloys through the addition of rare earth metals. J Mater Process Technol 33:5015–5023. https://doi.org/10.1023/A:1004463125340

43. Lasagni F, Mingler B, Dumont M, Degischer HP (2008) Precipitation kinetics of Si in aluminium alloys. Mater Sci Eng A 480:383–391. https://doi.org/10.1016/j.msea.2007.07.008

44. Jia YD, Cao FY, Scudino S, Ma P, Li HC, Yu L, Eckert J, Sun JF (2014) Microstructure and thermal expansion behavior of spray-deposited Al-50Si. Mater Des 57:585–591. https://doi.org/10.1016/j.matdes.2013.12.066

45. Ren SB, He XB, Qu XH, Humail IS, Li Y (2007) Effect of Mg and Si in the aluminum on the thermo-mechanical properties of pressureless infiltrated SiCp/Al composites. Compos Sci

Technol 67:2103–2113. https://doi.org/10.1016/j.compscitech.2006.11.006

46. Tayebi M, Jozdani M, Mirhadi M (2019) Thermal expansion behaviour of Al-B4C composites by powder metallurgy. J Alloys Compd 809:151753. https://doi.org/10.1016/j.jallcom.2019.151753

47. Jiang T, Li SJ, Yu C, Fu JY, Wei BW, Luo LL, Xu GM (2019) The evolution on the microstructure and thermal expansion behavior of Al-50Si alloy with different P contents. J Mater Sci-Mater EL 30:6786–6794. https://doi.org/10.1007/s10854-019-00990-1